

CO line ratios in molecular clouds: the impact of environment

Camilo H. Peñaloza¹, Paul C. Clark¹, Simon C.O. Glover²,
& Ralf S. Klessen^{2,3}

¹*School of Physics and Astronomy, The Queens Buildings, The Parade, Cardiff University, Cardiff CF24 3AA, UK*

²*Universität Heidelberg, Zentrum für Astronomie, Institut für Theoretische Astrophysik, Albert-Ueberle-Str. 2, 69120 Heidelberg, Germany*

³*Universität Heidelberg, Interdisziplinäres Zentrum für Wissenschaftliches Rechnen, INF 205, 69120 Heidelberg*

7 June 2021

ABSTRACT

Line emission is strongly dependent on the local environmental conditions in which the emitting tracers reside. In this work, we focus on modelling the CO emission from simulated giant molecular clouds (GMCs), and study the variations in the resulting line ratios arising from the emission from the $J = 1 - 0$, $J = 2 - 1$ and $J = 3 - 2$ transitions. We perform a set of smoothed particle hydrodynamics (SPH) simulations with time-dependent chemistry, in which environmental conditions – including total cloud mass, density, size, velocity dispersion, metallicity, interstellar radiation field (ISRF) and the cosmic ray ionisation rate (CRIR) – were systematically varied. The simulations were then post-processed using radiative transfer to produce synthetic emission maps in the 3 transitions quoted above. We find that the cloud-averaged values of the line ratios can vary by up to ± 0.3 dex, triggered by changes in the environmental conditions. Changes in the ISRF and/or in the CRIR have the largest impact on line ratios since they directly affect the abundance, temperature and distribution of CO-rich gas within the clouds. We show that the standard methods used to convert CO emission to H_2 column density can underestimate the total H_2 molecular gas in GMCs by factors of 2 or 3, depending on the environmental conditions in the clouds.

Key words: Star formation, ISM, CO emission, molecular clouds

1 INTRODUCTION

The evolution, structure and physical properties of giant molecular clouds (GMCs) are highly dependant on the surrounding environmental conditions. The changes in the surrounding environment of GMCs can have a direct impact on the formation of stars, since it is within these complicated cloud complexes that most of the molecular gas, which eventually will be transformed into stars, is contained (Klessen & Glover 2016). Gas is mostly found in the form of molecular hydrogen (H_2) that due to the low temperatures of GMCs cannot be directly observed. Therefore empirically derived relations help estimate the total molecular content by making use of other molecular tracers.

Carbon monoxide's (CO) easily excited rotational lines make it one of the most well known tracers of the interstellar medium (ISM), as such we rely on CO emission to estimate the total molecular content of a GMC. The X-factor (X_{CO}) allows us to estimate the total molecular gas of a GMC from the integrated intensity of the $J = 1 - 0$ emission line of CO by

$$N_{H_2} = X_{CO} W_{10}, \quad (1)$$

where N_{H_2} is the column density of H_2 , W_{10} the integrated intensity of the $J = 1 - 0$ transition of CO and X_{CO} the empirically derived conversion factor. Several studies have already explored the accuracy of X_{CO} and its dependence on environmental conditions (Bolatto, Wolfire & Leroy 2013; Papadopoulos et al. 2012; Sandstrom et al. 2013; Offner et al. 2014; Clark & Glover 2015; Barnes et al. 2015).

As distances become larger, it becomes harder to resolve far away clouds in nearby galaxies. Extragalactic studies therefore rely on higher rotational transitions with smaller wavelengths since they permit higher-resolution imaging. Most commonly used are the $J = 2 - 1$ and $J = 3 - 2$ rotational transition lines since they are bright and easily observed. The drawback however is that X_{CO} is an empirical relation that is only calibrated for the $J = 1 - 0$ emission line. Therefore, the integrated intensity of $J = 2 - 1$ emission line (W_{21}) is converted to W_{10} by using the empirically

derived ratio $R_{21} = W_{21}/W_{10}$. Similarly the empirically derived $R_{31} = W_{32}/W_{10}$ is used to convert from W_{32} to W_{10} . One then applies the X-factor to convert the CO emission into a column density of H_2 .

The ratios R_{21} and R_{31} thus play a key role in our understanding of galactic-scale star formation relations, such as the Kennicutt-Schmidt relationship (Schmidt 1959; Kennicutt 1998). Typically, extragalactic studies adopt a value of $R_{21} = 0.7$ (Eckart et al. 1990; Casoli et al. 1991; Brand & Wouterloot 1995; Sakamoto et al. 1997; Hasegawa 1997; Sawada et al. 2001; Bigiel et al. 2008; Leroy et al. 2009; Barriault, Joncas & Plume 2011) to convert from W_{21} to W_{10} . However, this could be inaccurate given the results shown in Peñaloza et al. (2017), which suggest R_{21} has a bimodal distribution dependant on the physical conditions surrounding the emitting gas. Another example of a widely-used ratio is R_{31} , which is mostly used to study star formation in high redshift galaxies (Aravena et al. 2010; Bauermeister et al. 2013; Aravena et al. 2014; Daddi et al. 2015). In most of these cases the $J = 3 - 2$ emission line is observed and then converted using the standard value $R_{31} = 0.5$ (Aravena et al. 2014), before deriving any physical properties of the system.

Fortunately numerical simulations provide a way through which these ratios can be studied and their behaviour and dependancies on environment properly quantified. In this paper we numerically follow the evolution of GMCs that are post-processed to generate synthetic observations. The aim is to gain a better understanding of the ratios of CO's rotational emission lines and how they are influenced by changes in cloud mass, density, metallicity, the strength of the Interstellar Radiation Field (ISRF) and the cosmic ray ionization rate (CRIR). Therefore we simulate a set of clouds in which the initial conditions are systematically changed in order to cover a wide range of realistic environmental conditions.

The structure of the paper is as follows. In section 2 we describe the numerical setup and the initial conditions used to model the evolution and synthetic observations of these GMCs. In Section 3 we present our results. We look at how the cloud's morphology changes depending on environment as well as study the impact this has on the value and distribution of R_{21} . In Section 4 we examine how variations in environment impact the observation of unresolved GMCs and the consequences this has on different line ratios. In Section 5 we discuss how variations in R_{21} and R_{31} affect calculated column densities of H_2 as well as whether R_{21} can trace changes in CO abundances. Finally we summarise our findings in Section 6.

2 METHOD

2.1 Hydrodynamics and chemistry

To model the gas in this study, we use a modified version of the publicly available smoothed particle hydrodynamics (SPH) code, GADGET-2 (Springel 2005). These modifications include a time-dependent chemical network that follows the formation and destruction of H_2 (Glover & Mac Low 2007a,b) and CO (Nelson & Langer 1999), more details of which can be found in Glover & Clark

(2012a), which also includes the photodissociation rates that we adopt in this study. We adopt the same radiative heating and cooling rates, and cosmic ray heating rate as described in Glover & Mac Low (2007a) and Glover & Clark (2012b). To treat the attenuation of the ISRF we use the TREECOL algorithm developed by Clark, Glover & Klessen (2012).

2.2 Initial conditions

We produce a set of numerical simulations with different initial conditions to study the impact of environment on the evolution of GMCs and the impact this has on CO emission lines. The initial setup of all the clouds is a uniform sphere where a turbulent velocity field with a power spectrum of $P(k) \propto k^{-4}$ is imposed and left to decay as the cloud evolves. Since the aim of this study is to look at the structure and evolution of GMCs prior to the onset of star formation, we therefore stop each run just before the onset of star formation modelled by the creation of so called sink particles (see Glover & Clark 2012b). It is important to note that since the initial conditions affect the evolution of each cloud, when star formation is triggered will be at different times for each run. We make use of the clouds simulated in previous papers by Clark & Glover (2015) and Glover & Clark (2016) since they already cover part of the parameter space we intend to study. Below we cover what the variations in initial conditions are but refer the reader to those papers for full details.

First we summarise the initial conditions of the simulations by Clark & Glover (2015). They cover a range of different ISRFs intensities that are scaled proportional to G_0 , where $G_0 = 1.7$ in Habing (1968) units and a range of CRIRs that are scaled proportional to $\zeta_H = 3 \times 10^{-17} \text{ s}^{-1}$. These clouds have a mass of either $10^4 M_\odot$ or $10^5 M_\odot$. Additionally the initial density is varied to be either $n = 100 \text{ cm}^{-3}$ or $n = 10^4 \text{ cm}^{-3}$. Lastly since the initial state of the gas can delay the formation of CO and therefore its total emission, the initial molecular fraction is changed to be either $f(H_2) = 1$ or $f(H_2) = 0$, i.e. fully molecular or fully atomic. All of these runs were performed with a turbulent velocity field generated from a 'natural' mix of solenoidal and compressive modes in a 2:1 ratio.

The simulations by Glover & Clark (2016) have an initial mass of $10^4 M_\odot$, initial density of $n = 276 \text{ cm}^{-3}$, have an initial molecular fraction of $f(H_2) = 0$ and have a turbulent velocity field that is generated from purely solenoidal modes. In addition the ISRF and CRIR are scaled in the same way as Clark & Glover (2015), however the CRIR is scaled proportional to $\zeta_H = 1 \times 10^{-17} \text{ s}^{-1}$. Finally the metal fraction is varied with respect to solar metallicity (Z_\odot), adopting values of $Z = Z_\odot$, $Z = 0.5 Z_\odot$ and $Z = 0.2 Z_\odot$.

Taken together, these two sets of simulations cover a wide range of parameter space. However, there are still cases where it is difficult to compare the clouds, as several cloud properties are changing at once. To isolate the effect of varying individual environmental properties, we thus perform an additional set of simulations for our current study. First, Clark & Glover (2015) and Glover & Clark (2016) scale the ISRF and CRIR *together* making it hard to disentangle the effect of either, therefore we run four clouds that vary either the ISRF or the CRIR. Additionally the small mass clouds in Clark & Glover (2015) and all of the clouds in

Glover & Clark (2016) have a slightly different initial density, different turbulent velocity field, a different α_{vir} and slightly different ζ_H . As such we present four extra simulations where only one of these parameters is varied.

Note that the dynamical state of our clouds is primarily controlled by the ratio of gravitational to (turbulent) kinetic energy. In all our clouds the thermal energy in the gas is insufficient to unbind the cloud, even in the cases where we adopt high ISRFs and high CRIRs. For more details one can also see the study by Bertram et al. (2015) where they explore the binding and star-forming properties of cloud that are exposed to even higher ISRFs and CRIRs than we adopt here. In addition, clouds from Glover & Clark (2016) apply an external pressure term to prevent “evaporation” of material (Benz 1990). However we find that the external pressure has minimal influence on whether our clouds will collapse and form stars.

We summarise the set of simulations in Table 1. Note that the IDs given in this table will be used throughout the rest of the paper.

2.3 Post-processing

Once the hydrodynamical simulation is finished we post-process the snapshot with RADMC-3D (Dullemond 2012) and create synthetic images. Given that we have clouds of different sizes and densities, we used the refining method developed in Peñaloza et al. (2017) to account for all particles in the GADGET-2 snapshot. This assures that no information is lost when interpolating particles to the grid and therefore guarantees convergence of the intensity maps which is important when comparing line ratios of different sized clouds. Additionally, we have implemented an extension to the ‘Sobolev’ approximation in RADMC-3D (Shetty et al. 2011), that accounts for both the velocity and density variations within the cloud. By making use of density gradients within the cloud we can better calculate the local optical depth and therefore the total emission for the cloud. A more detailed description is given in Appendix A. Since radiative transfer simulations of clouds in Clark & Glover (2015) and Glover & Clark (2016) were performed without these additional methods, we re-do the radiative transfer for these clouds.

For each cloud we create synthetic observations for the first three rotational lines of ^{12}CO ($J = 1 - 0$, $J = 2 - 1$, $J = 3 - 2$). Integrating along the z -axis i.e. velocity in PPV space, we then create zeroth moment maps for each line. All the final maps have an imposed cut at emissions lower than 0.01 K km s^{-1} , this is motivated by our previous study (Peñaloza et al. 2017). All these maps are ‘ideal’ synthetic observations since they do not include any noise or telescope effects.

Finally it is worth noting that we only study the first three rotational lines of CO since higher transitions depend on additional physics that are not well-captured by this type of numerical simulation. Higher CO transitions are normally excited by high velocity shocks within the clouds (Pellegrini et al. 2013; Pon et al. 2016); these shocks are not well resolved by 3D numerical simulations, and so the microphysics of such regions are not properly traced by our models.

3 RESULTS

3.1 Cloud morphology and appearance

To qualitatively illustrate how the cloud morphology changes, Figure 1 contains the following simulations CG15-M4-G1, CG15-M5-G1, CG15-M5-G100 and GC16-Z1-G1. In the upper panels of Figure 1 we present the column densities at the time when the synthetic observations are created. The fact that these simulations all used the same random seed in the turbulent initial velocity field is evident in the column densities images. The middle panels show the synthetic observations for the ^{12}CO ($J = 2 - 1$) line. The synthetic observations are able to recover the general structure of the cloud, however, the filamentary structures seen in the column density maps are not as easily identified in the emission maps, due to the optically-thick nature of the CO emission lines.

Comparing the first two columns of Figure 1 reveals how changing the mass of the cloud alters their emission. By increasing the mass by a factor of 10, but maintaining the initial density, the size of the cloud is effectively doubled. Since the initial virial state of the simulations is the same, the initial velocity dispersion is roughly 5 times higher in CG15-M5-G1 than in CG15-M4-G1. As the sound speed of the gas is similar in the two simulations, the higher-mass cloud has Mach number 4-5 times higher than the low mass cloud. As a consequence, the higher-mass cloud has a more intricate web-like structure with a larger number of turbulence driven filaments. This is reflected in the synthetic images of the emission, since high density regions correlate with high intensity regions and vice-versa, and as we shall see this is an important factor in the distribution of R_{21} .

The middle two columns compare the effect of varying the ISFR and the CRIR. In the high ISRF/CRIR scenario most of low-density, poorly-shielded CO has been dissociated and the thin, low density filaments have completely disappeared. More evident in the synthetic observations is how the apparent size of the cloud has been reduced by removing the low intensity regions that were previously enveloping the entire cloud.

Finally the bottom panels of Figure 1 contain the R_{21} maps. As shown by Peñaloza et al. (2017), the area-weighted PDF of R_{21} has a bimodal distribution, with peaks centred at $R_{21} \sim 0.3$ and $R_{21} \sim 0.7$. In the first two columns, it is clear that the ratio map is mostly dominated by values of $R_{21} \sim 0.7$, nonetheless lower values of R_{21} are present in regions where $W_{21} < \text{few K km s}^{-1}$. A very different picture is seen in the R_{21} map for CG15-M5-G100: towards the centre of the cloud $R_{21} \sim 0.5 - 0.7$ but at the outskirts of the cloud $R_{21} > 1$. The high ISRF results in very high temperatures ($T > 40\text{K}$) at the edge of very dense ($n > 10^3 \text{ cm}^{-3}$) regions of the cloud. In such circumstances, the $\tau = 1$ surface for $J = 1 - 0$ can be deeper into the cloud than the $\tau = 1$ surface for $J = 2 - 1$, which can result in $R_{21} > 1$. This effect was demonstrated in the 1-D models of Sakamoto et al. (1994). It is worth noting that R_{21} can also be larger than 1 when the source of radiation is embedded within the cloud (see Figure 11 from Nishimura et al. 2015). Finally when comparing R_{21} between CG15-M4-G1 and GC16-Z1-G1 it is clear that the morphology of the cloud (and thus the choice of turbulent velocity field) has an impact on the final value of R_{21} .

Qualitatively the ISRF and the CRIR have the biggest

ID	n	M	α_{vir}	ISRF	CRIR	$f(\text{H}_2)$	Z	Turbulence	Time ^a
	[cm^{-3}]	[M_{\odot}]		[G_0]	[10^{-17} s^{-1}]		[Z_{\odot}]		[Myr]/[t_{ff}]/[t_{cr}]
Clark & Glover (2015)									
CG15-M4-G1	100	10^4	0.5	1	3	1	1	Natural	1.83/0.42/0.60
CG15-M4-G10	100	10^4	0.5	10	30	1	1	Natural	2.09/0.48/0.69
CG15-M4-G100	100	10^4	0.5	100	300	1	1	Natural	1.96/0.45/0.65
CG15-M5-G1	100	10^5	0.5	1	3	1	1	Natural	1.17/0.27/0.39
CG15-M5-G10	100	10^5	0.5	10	30	1	1	Natural	1.52/0.35/0.50
CG15-M5-G100	100	10^5	0.5	100	300	1	1	Natural	1.39/0.45/0.65
CG15-M5-G1/A	100	10^5	0.5	1	3	0	1	Natural	1.31/0.30/0.43
CG15-M5-G100/A	100	10^5	0.5	100	300	0	1	Natural	1.26/0.29/0.42
CG15-CMZ1	10^4	10^5	0.5	100	300	1	1	Natural	0.10/0.23/0.67
CG15-CMZ2	10^4	10^5	2	100	300	1	1	Natural	0.09/0.22/0.32
Glover & Clark (2016)									
GC16-Z1-G1	276	10^4	1	1	1	0	1	Solenoidal	1.97/0.75/1.53
GC16-Z1-G10	276	10^4	1	10	10	0	1	Solenoidal	2.17/0.83/1.68
GC16-Z1-G100	276	10^4	1	100	100	0	1	Solenoidal	2.03/0.78/1.57
GC16-Z05-G1	276	10^4	1	1	1	0	0.5	Solenoidal	2.44/0.93/1.89
GC16-Z05-G10	276	10^4	1	10	10	0	0.5	Solenoidal	2.61/1.00/2.02
GC16-Z05-G100	276	10^4	1	100	100	0	0.5	Solenoidal	2.81/1.07/2.18
GC16-Z02-G1	276	10^4	1	1	1	0	0.2	Solenoidal	2.79/1.06/2.16
GC16-Z02-G10	276	10^4	1	10	10	0	0.2	Solenoidal	2.95/1.13/2.29
GC16-Z02-G100	276	10^4	1	100	100	0	0.2	Solenoidal	3.59/1.37/2.78
Additional Runs									
M4-G1-CR30	100	10^4	0.5	1	30	1	1	Natural	2.00/0.46/0.66
M4-G1-CR300	100	10^4	0.5	1	300	1	1	Natural	2.35/0.54/0.77
M4-G10-CR3	100	10^4	0.5	10	3	1	1	Natural	2.09/0.48/0.69
M4-G100-CR3	100	10^4	0.5	100	3	1	1	Natural	2.13/0.49/0.70
M4-G1-CR1	100	10^4	0.5	1	1	1	1	Natural	1.78/0.41/0.59
M4- α 1	100	10^4	1	1	3	1	1	Natural	1.87/0.43/0.87
M4-N300	300	10^4	0.5	1	3	1	1	Natural	0.73/0.29/0.42
M4-SOL	100	10^4	0.5	1	3	1	1	Solenoidal	3.13/0.72/1.03

Table 1. In this table we summarise the initial conditions for each cloud. The virial conditions of the clouds are given by $\alpha_{vir} = E_{kin}/E_{pot}$. G_0 is given in Habing (1968) units. $f(\text{H}_2)$ denotes the initial molecular fraction of the gas and Z_{\odot} its metallicity.

^a Run time/fraction of free-fall time/fraction of crossing time ($t_{cr} = R/\langle v \rangle$)

impact on R_{21} 's value and distribution. Their combined effects can hinder the accuracy of adopting a constant value of $R_{21} \sim 0.7$ and therefore over or underestimate the derived value for W_{10} .

3.2 Systematic dependences of R_{21}

The morphology of the cloud gives a qualitative picture of the impact that initial mass, turbulence and the ISRF/CRIR have on the CO emission and the corresponding line ratios. In this section we focus on the R_{21} line ratio. The different effects on the line ratio can be quantified by plotting the cumulative PDF of R_{21} weighted by integrated intensity (Figure 2). The separation between the curves for each cloud shows how changes in environmental conditions impact the distribution and average value of R_{21} . We reiterate here that low values of R_{21} ($\sim 0.2 - 0.4$) are associated with warm and diffuse gas, while high values of the R_{21} ($\sim 0.6 - 0.8$) are associated with cold and dense gas (Peñaloza et al. 2017).

3.2.1 The ISFR and the CRIR

The top left panel of Figure 2 plots the cumulative PDF for a set of the low mass clouds at solar metallicities. As the ISFR and the CRIR increase (solid lines), a larger fraction of the overall emission is associated with larger values of R_{21} . In this case almost half of the emission is associated with line

ratio values of $R_{21} > 1$. As the ISRF increases the unshielded molecular gas is fully dissociated, destroying most of the CO in the already diffuse gas and therefore resulting in no CO emission from these regions of the cloud. This is consistent with the fact that lower values of R_{21} (~ 0.3) are associated with diffuse and warm areas of the cloud (Sakamoto et al. 1994; Peñaloza et al. 2017). Similar to CG15-M5-G100 (see bottom left panel and Figure 1), values of $R_{21} > 1$ are correlated with CO emission originating from dense and hot gas at the edge of the cloud.

The dashed-dotted lines represent the runs where only the ISRF field was increased while the CRIR was left unchanged. For these clouds a large fraction of the emission is also associated with higher line ratios. However, a larger fraction (about 80 %) of the overall emission is associated with line ratios of $R_{21} \sim 0.6 - 0.8$. A smaller CRIR means the dense gas within the shielded regions of the cloud is not being heated and therefore results in a more compact cloud. As such most of the emission originates from dense and cold gas, which explains why a larger fraction of the emission is correlated with $R_{21} \sim 0.7$.

On the other hand the dashed lines represent the clouds where the ISRF was left constant while the CRIR were increased. In this case about 50 % of the overall emission is correlated with lower line ratios ($R_{21} \sim 0.3 - 0.6$). As shown by Glover & Clark (2016) (see also Bisbas, Papadopoulos & Viti 2015; Bisbas et al. 2017), an

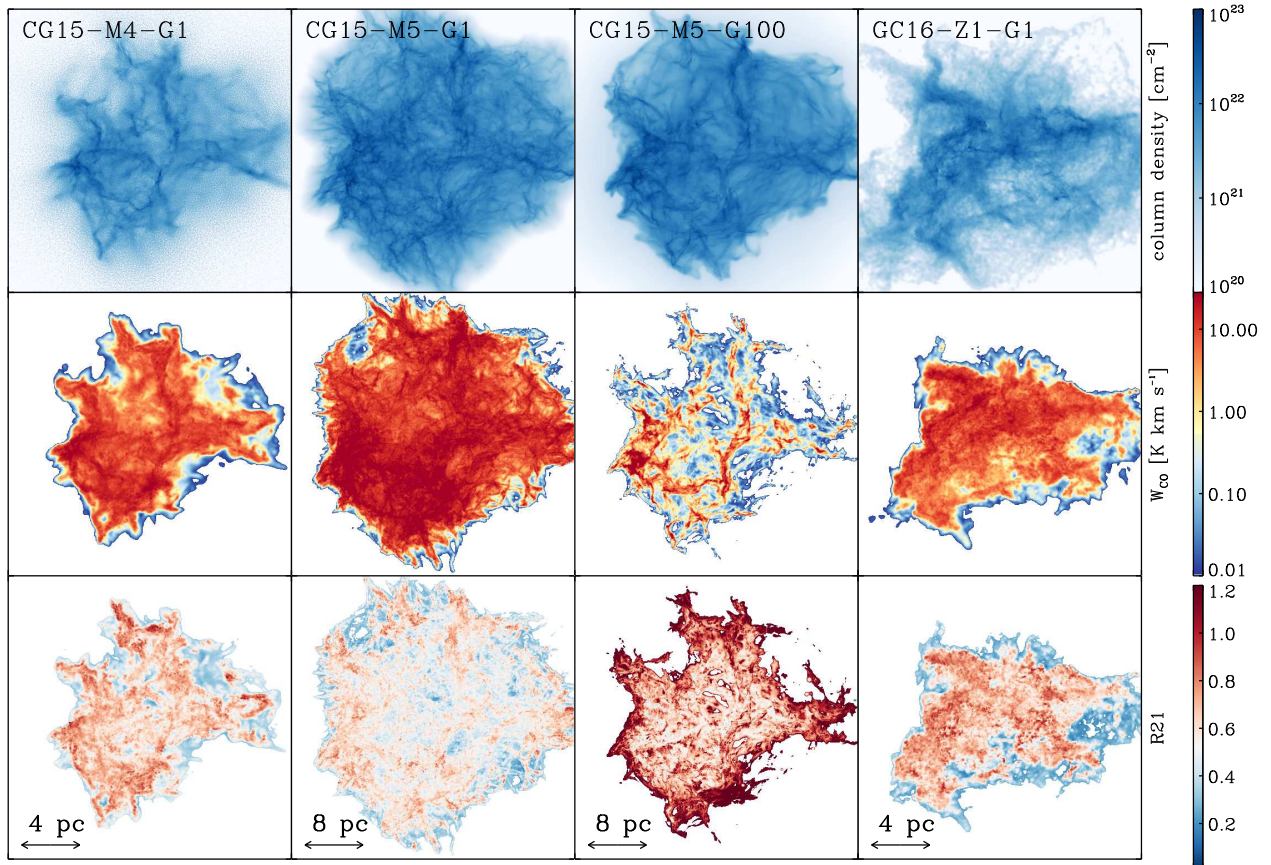


Figure 1. Top row: Column density maps for simulations CG15-M4-G1, CG15-M5-G1, CG15-M5-G100 and GC16-Z1-G1. Middle row: The integrated intensity of the CO $J = 2 - 1$ transition for each simulation. Bottom row: The ratio, R_{21} , of the integrated intensity of the CO $J = 2 - 1$ and $J = 1 - 0$ transitions for each simulation.

increase in ζ_H can lead to a decrease in CO abundance. Even though the total abundance of CO has been reduced it is still well shielded from the UV rays, resulting in emission originating from low density gas and therefore associated with lower line ratio values. The effect of ζ_H on CO abundance will be more thoroughly discussed in Section 5. Additionally, the high CRIR will heat up dense regions of the cloud, thereby increasing the overall emission associated with higher line ratios ($R_{21} > 0.9$).

Finally, by comparing the bottom left panel with the top left panel, we can see that the compound effect of the ISRF and the CRIR does not depend on the cloud mass. Although the higher mass clouds tend to contain more filamentary structures (as discussed in the previous Section), the combination of high ISRF and high CRIR results in heating which acts to smear out these high-density structures in both cases. As such, the variation in R_{21} as function of ISRF + CRIR looks very similar in the high- and low-mass clouds.

3.2.2 Metallicity

The top right panel of Figure 2 plots the cumulative PDF of low-mass clouds ($10^4 M_\odot$), with a solenoidal turbulent

seed and varying metallicities. By reducing the metallicity, the conditions to form CO tend to only be achieved within dense cores (Glover & Clark 2016), which results in less CO emission from diffuse regions of the cloud. This can reduce the percentage of the low values of R_{21} that are associated with low density gas, and indeed we see that in the case of $Z = 0.2 Z_\odot$, there is almost no emission associated with $R_{21} < 0.4$.

We also see variations in the fractions of emission associated with the higher R_{21} values, although the overall effect is still quite small. These variations are likely due to the fact that as we decrease the metallicity, the abundance of both CO and H_2 (the dominant collisional partner for CO) are both decreasing. As such, for a given total density of gas, the *effective* density of the species contributing to the emission is falling as we decrease the metallicity, which has the result of reducing R_{21} . However, this is going to be partly offset by the fact that the gas is hotter at lower metallicities, which acts to raise R_{21} , potentially explaining the overall small variation in the cumulative distribution of R_{21} .

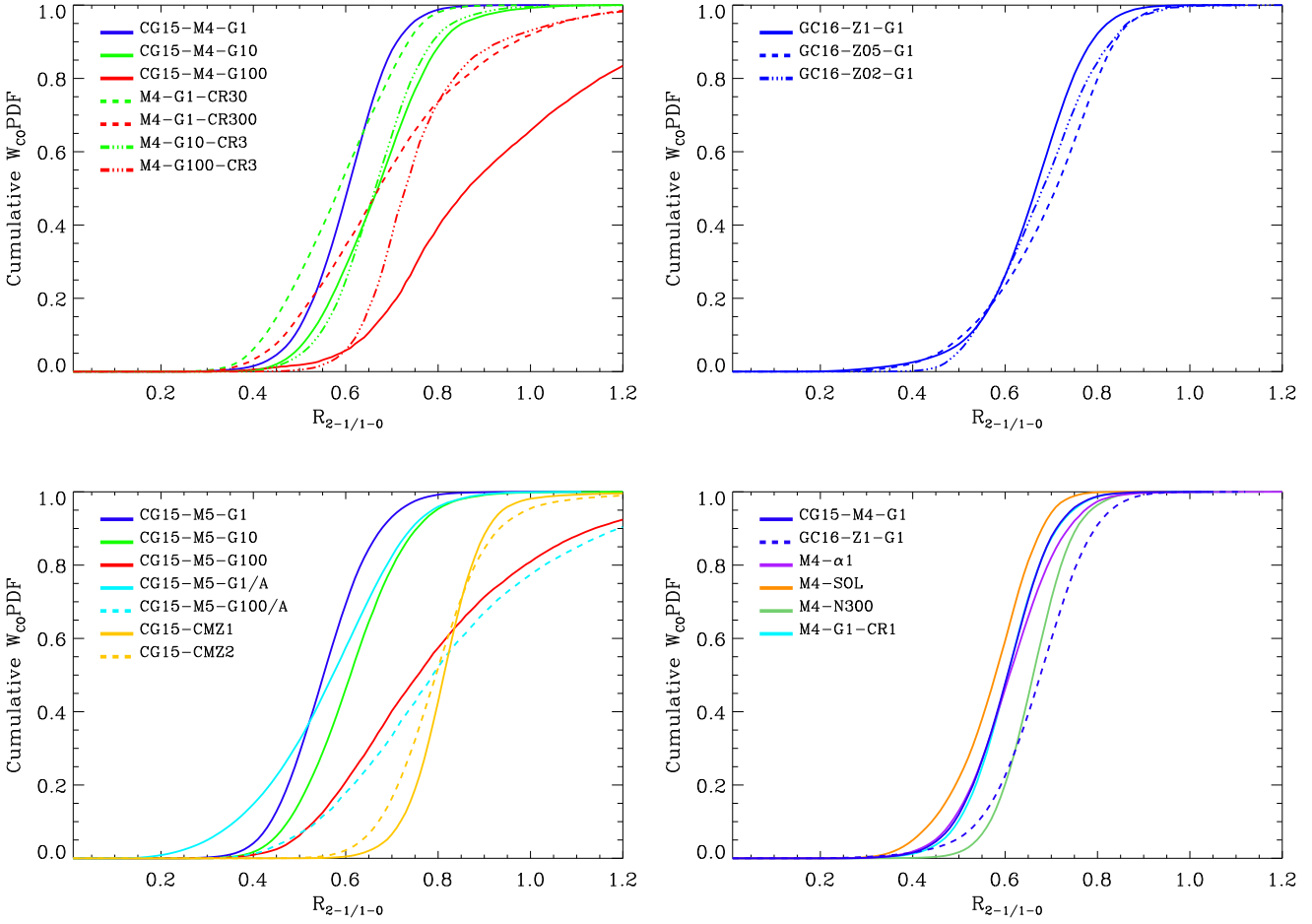


Figure 2. The cumulative PDF of R_{21} weighted by W_{CO} for different sets of clouds grouped by variations in their physical parameters. Top left: Small clouds ($10^4 M_{\odot}$), at solar metallicities and with varying ISRF, CRIR or both. Top right panel: Small clouds ($10^4 M_{\odot}$), with a solenoidal turbulent seed and varying metallicities. Bottom left panel: Large clouds ($10^5 M_{\odot}$) with variations in both ISFR and CRIR. Cyan lines are clouds that start atomic and yellow lines clouds with initial $n = 10^4 \text{ cm}^{-3}$. Bottom right panel: Small clouds ($10^4 M_{\odot}$) with changes to α_{vir} , initial density or the turbulent seed

3.2.3 Mass and molecular fraction

The bottom left panel of Figure 2 contains all the clouds with total mass of $10^5 M_{\odot}$. The first point to notice is, by comparing the blue lines in the top and bottom left panels, that increasing the total mass of the cloud leaves the overall value and distribution of R_{21} relatively unchanged.

The effect of having an initially atomic cloud is on the fraction of the overall gas associated with lower line ratios, where about 40 % of the emission has values of $R_{21} < 0.5$ for clouds that start fully atomic. This tail at low values of R_{21} is correlated with a larger fraction of the emission coming from low density/high temperature regions. This is consistent with the idea that less molecular material at the beginning will delay the formation of CO (Glover & Clark 2012b), resulting in lower column densities of CO. Given that the impact of the ISRF and the CRIR are much stronger, as discussed above, the effect of initial $f(\text{H}_2)$ can be more easily observed at low ISRF, as the high-ISRF cases (solid red and dashed cyan) are relatively similar.

Finally the two CMZ-like runs with an initial density

of $n = 10^4 \text{ cm}^{-3}$ have a larger average value of R_{21} , where most of the overall emission is associated with $R_{21} \sim 0.8$. This is due to the fact that the initial density is well above the critical density of the first two rotational transition lines of CO ($n_{\text{crit},1-0} \approx 2000 \text{ cm}^{-3}$, $n_{\text{crit},2-1} \approx 10^4 \text{ cm}^{-3}$). As a result the gas is well shielded from the ISRF and CO is easily excited. Since most of the emission is originating from high density gas, this means that R_{21} will be centred near ~ 0.7 .

3.2.4 Turbulence, α_{vir} and initial density

As mentioned before we have used clouds from Clark & Glover (2015) and Glover & Clark (2016), however as it can be seen in Table 1 that these have slightly different initial conditions and environmental parameters. The bottom right panel of Figure 2 shows the clouds that explore variations in only these features. First we must note that even though CG15-M4-G1 (blue solid line) and GC16-Z1-G1 (blue dashed line) have very similar initial conditions, the changes in turbulence, α_{vir} and initial density still noticeably change R_{21} 's distribution.

Glover & Clark (2016) adopted a solenoidal velocity field. Such a field has no compressive motions ($\nabla \cdot \mathbf{u} = 0$), resulting in more flocculent cloud (lower density) with a narrower PDF than is found for fields with similar Mach numbers and power spectra, but which contain compressive modes (Federrath et al. 2010). Consequently, a larger fraction of the emission originates from more diffuse gas, which is correlated with lower values of R_{21} in the clouds which adopt a solenoidal velocity field.

Increasing the value of α_{vir} slightly increases the average value of R_{21} . A larger kinetic energy results in higher Mach numbers, and thus more shock-compressed high-density regions. Although the higher α_{vir} will also cause the clouds to expand, which would lower R_{21} , there is not sufficient time for this to occur in our study; these clouds form stars more rapidly than the lower α_{vir} clouds, which means we post-process them at an earlier time, before they have had the chance to expand. The net effect is more gas is at high densities when we come to post-process, and thus a slightly larger fraction of the cloud will be associated with larger values of R_{21} . Clearly this effect will depend on time, which is beyond the scope of this study.

The green line shows, to a lesser extent, what was observed for CMZ-like clouds; increasing the initial density reduces the amount of diffuse gas and effectively increases the fraction of the gas associated with higher values of R_{21} . The slightly different ζ_{H} between CG15-M4-G1 and GC16-Z1-G1 has very little effect, this can be seen by the cyan line where $\zeta_{\text{H}} = 1 \times 10^{-17} \text{s}^{-1}$. Given that the variation in ζ_{H} is small the change in R_{21} is not substantial. However reducing the CRIR does slightly reduce the amount of emission associated with low line ratios. Finally, we note that the combined effect of turbulence, α_{vir} , initial density and slightly different ζ_{H} explain the different average value and distribution of R_{21} between CG15-M4-G1 and GC16-Z1-G1.

4 R_{21} FROM OBSERVATIONALLY UNRESOLVED CLOUDS

The previous section explained how variations in the initial conditions and in the surrounding environment affect both the mean value and distribution of R_{21} . Moreover, effects on R_{21} can be associated with different regions of the cloud and are correlated with local physical properties of the gas. However, when comparing to observations in an extragalactic context, where R_{21} is used as a conversion factor, details about the varying value of R_{21} within molecular clouds are not known. In this context one of our clouds will most likely be smaller than the observational beam size (c.f. Bigiel et al. 2016; Schinnerer et al. 2013) and therefore the total intensity of a one or more GMCs will be averaged within this beam. Therefore to study R_{21} in the context of observationally unresolved clouds, we first take the area-weighted intensity average of each cloud for each rotational transition line and then take the ratio of the two averaged intensities. In this section we focus on presenting the results from these area-averaged line ratios.

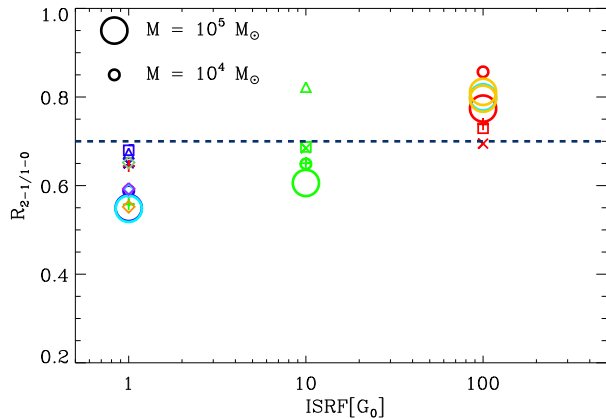


Figure 3. The averaged value of R_{21} for each cloud as a function of their respective ISRF (G_0). Large circles represent clouds that have a mass of $M = 10^5 M_{\odot}$ and small shapes represent clouds with a mass of $M = 10^4 M_{\odot}$. Blue, green and red shapes represent an increase of the ISRF and/or CRIR by 1, 10 or 100 respectively. Xs, squares and triangles represent metallicities of Z_{\odot} , $0.5Z_{\odot}$ and $0.2Z_{\odot}$ respectively. Large cyan circles denote an initial hydrogen fraction of $f(\text{H}_2) = 0$. Yellow circles are the two runs with an initial number density of $n = 10^4 \text{cm}^{-3}$. Plus signs are clouds where the ISRF and the CRIR have been varied independently. Diamonds are the additional runs plotted in the bottom right panel of Figure 2 and have the same colours. Finally the dashed line represents the standard value used for converting W_{21} to W_{10} . Note: we have not included GC16-Z02-G100 since the gas is not able to form enough molecular gas and therefore produces almost no CO emission

4.1 Averaged R_{21} for the whole cloud

In the previous section it was suggested that varying the UV intensity has an impact on R_{21} . We therefore plot the area-averaged value of R_{21} against the ISRF for all the clouds in Figure 3.

First thing to note is that the averaged value of R_{21} covers a range of values between 0.5 – 0.9, this confirms that changes in the cloud’s environmental conditions do influence the overall value of R_{21} . An increasing ISRF is directly correlated with an increase in the average value of R_{21} . Additionally, within each ISRF bin there is appreciable scatter, which can be attributed to the different changes in environmental conditions discussed in the previous Section. However, since the plot shows an averaged value for R_{21} , the specific changes in the distribution of R_{21} are reduced making it harder to distinguish between different environmental effects.

Extragalactic observations often use R_{21} as a conversion factor rather than a diagnostic tool for GMC structure. In that context the averaged dashed line in Figure 3 represents the observationally derived and most commonly used value of R_{21} (Eckart et al. 1990; Casoli et al. 1991; Brand & Wouterloot 1995; Sakamoto et al. 1997; Hasegawa 1997; Sawada et al. 2001; Bigiel et al. 2008; Leroy et al. 2009; Barriault, Joncas & Plume 2011). This line lies in the middle of the scatter of R_{21} values of our clouds, suggesting that $R_{21} \sim 0.7$ is a good first approximation for converting W_{21} into W_{10} . Nonetheless, it questions the reliability and robustness of the conversion factor, and suggests that adopt-

ing a fiducial value can lead to errors in derived quantities such as the total molecular gas. We discuss the consequences of such an approach, and possible solutions, in Section 5.

It is important to note that the agreement between our simulations and the accepted value of R_{21} improves when considering higher sensitivity cuts to our detection limits. Our synthetic observations have an already low emission cut of 0.01 K km s^{-1} , when we impose a detection limit of 5 K km s^{-1} instead the scatter is almost completely gone. Considering that the emission from diffuse gas associated with lower line ratios is always very faint, it follows that $R_{21} \sim 0.7$ as sensitivity is reduced. This is a consequence of R_{21} being derived in a galactic context where clouds are well resolved, and suggests that sensitivity plays an important role in how we have empirically derived the accepted value of R_{21} .

4.2 CO emission as a probe of physical conditions

Naturally CO emission is directly correlated to the temperature of CO molecular gas within the cloud. However, the overall temperature range probed by CO is not necessarily representative of the range of temperatures found in H_2 -rich gas. In the section, we explore whether CO emission, and more explicitly R_{21} , can accurately trace the gas temperature within GMCs. In order to compare to the averaged value of R_{21} calculated before, we define the cloud-averaged temperature as

$$\langle T \rangle = \frac{\sum_{i=1}^n m_i T_i \chi_i}{\sum_{i=1}^n m_i \chi_i} \quad (2)$$

where the sum is over all the SPH particles, m is the particle mass, T is the particle temperature and χ is the abundance of the molecule of interest. In this case we calculate the average temperature of H_2 (T_{H_2}) and of CO (T_{CO}). It is important to note that the T is the kinetic temperature of the gas obtained from the original SPH data that was the input for the radiative transfer.

In Figure 4 we plot $\langle T_{\text{H}_2} \rangle$ vs $\langle T_{\text{CO}} \rangle$ where every point represents a cloud and the points have the same shape and colour as in Figure 3. First thing to note is that the temperature of the molecular cloud – as defined by the H_2 – increases as we increase the ISRF and/or CRIR, which is to be expected. However this increase in temperature is only reflected in $\langle T_{\text{H}_2} \rangle$, while CO-rich gas never reaches temperatures above $T \sim 40 \text{ K}$. As such the CO emission from the cloud is only tracing the temperature variations in a sub-set of the full H_2 molecular gas. This is easily understood since the bulk of the CO gas is within well-shielded regions where temperature of the gas is low and the densities are above n_{crit} . This is not the case for H_2 , which is present in more diffuse regions where the temperature range can be higher (see also Walch et al. 2015 and Glover & Smith 2016 who find similar results in larger-scale simulations of the ISM).

One notable exception is when considering the two CMZ clouds (yellow circles), in this case T_{CO} and T_{H_2} are very similar. Since the initial density of these clouds is much higher, this results in most of the gas being well shielded and therefore at similar temperatures. Since the densities

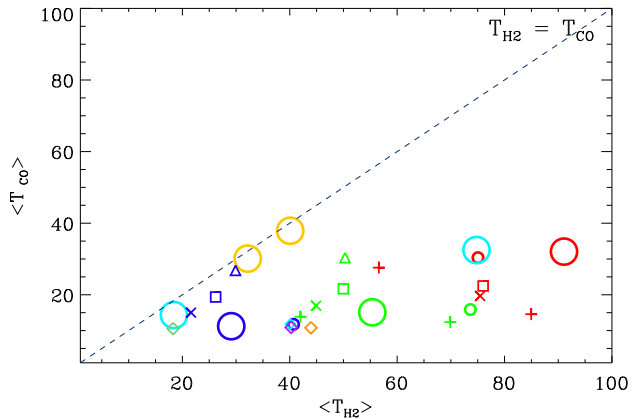


Figure 4. The average temperature of H_2 as calculated by equation 2 plotted against the average temperature of CO. Each point represents a cloud and has the same colour and shapes as in Figure 3

are high enough to excite CO then the CO emission is well correlated with the overall temperature of the gas. As was mentioned in the previous Section this is also reflected in the small variations of R_{21} .

4.3 Alternative line ratios

Having created synthetic observations for the lowest three emission lines of CO’s rotational ladder, it is a simple task to consider other ratios between these lines as possible conversion factors. In this section we explore the ratios R_{32} and R_{31} , which have both been employed as conversion factors in extragalactic studies.

4.3.1 R_{32}

We first consider R_{32} , that is the ratio between the third ($J = 3 - 2$) and second ($J = 2 - 1$) rotational levels of CO. In order to judge how R_{32} varies we plot a similar figure to Figure 3, where we take the average intensities of each line for each cloud and then calculate the line-ratio. This is shown in Figure 5.

In this case the overall scatter is considerably larger than it was for R_{21} and our results are all above the standard value of $R_{32} = 0.5$ (Vlahakis et al. 2013). At the same time R_{32} is also highly dependent on the changes in the ISRF as demonstrated by the increase in the averaged value of R_{32} with increasing ISRF. When we examine the properties of the individual clouds within each ISRF bin, the spread seems to be correlated with the initial density of the simulations. Considering that the critical densities of $J = 2 - 1$ and $J = 3 - 2$ are of the same order of magnitude ($n_{\text{crit}} \sim 10^4 \text{ cm}^{-3}$) then a larger fraction of R_{32} ’s distribution originates from regions that are sub-critically excited i.e. $n < 10^4 \text{ cm}^{-3}$ with lower initial densities. This explains why the value of R_{32} is larger for most of the GC16 clouds that have a slightly larger initial density.

Finally the CMZ-like clouds have a larger value of $R_{32} \sim 0.9$. Since the cloud starts with an initial density of $n = 10^4 \text{ cm}^{-3}$, which is close to the critical densities for both

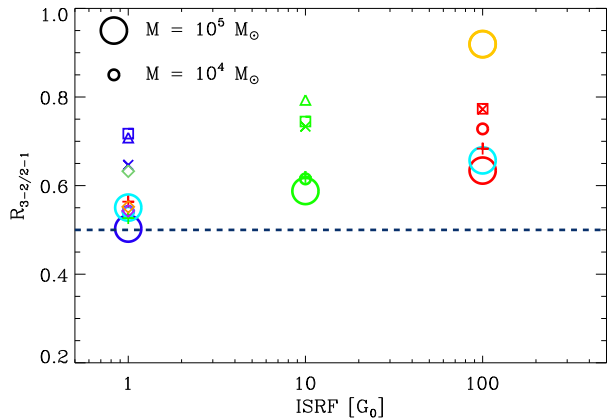


Figure 5. Similar to Figure 3 but for the ratio of the $J = 3 - 2$ and $J = 2 - 1$ rotational transition lines. Colour coding is the same as in Figure 3. The dashed line is the commonly used value for R_{32} (Vlahakis et al. 2013)

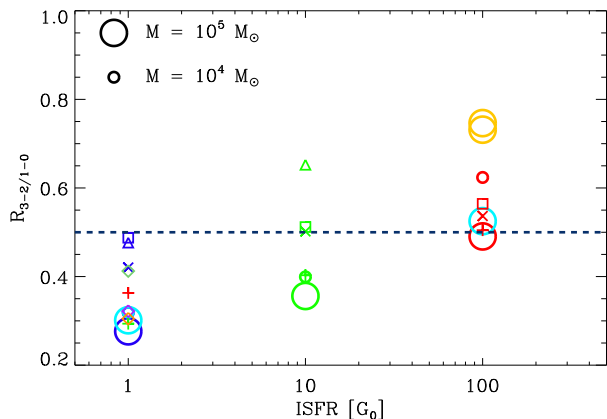


Figure 6. Similar to the top panel of Figure 3 but for $J = 3 - 2$ and $J = 1 - 0$ rotational transition lines. The dashed line represents the commonly used conversion factor for R_{31} (Aravena et al. 2014)

transitions, this results in comparable emission rates from both lines and therefore a ratio closer to unity.

4.3.2 R_{31}

In Figure 6 we look at the variations of R_{31} , that is the ratio between CO's third ($J = 3 - 2$) and first ($J = 1 - 0$) rotational emission lines. The scatter for R_{31} is similar to R_{32} and we also see an increase in the average value with increasing ISRF. However, the value of R_{31} is more evenly spread in each ISRF bin, suggesting that R_{31} is slightly more susceptible to changes of environment and initial conditions of GMCs.

The reason R_{31} has a higher variability is due to the larger difference in excitation conditions for both lines. The critical density of the $J = 3 - 2$ emission line is $n_{\text{crit}} = 3.6 \times 10^4 \text{ cm}^{-3}$ that is over an order of magnitude higher than the $J = 1 - 0$ line. Furthermore the difference in energy required to excite both lines is $\sim 27.7 \text{ K}$, which is quite

significant when considering the low temperature environments of dense regions within GMCs. This explains why at lower ISRF R_{31} is small, since a significant amount of emission is arising from diffuse regions where the $J = 1 - 0$ line is easily excited but $J = 3 - 2$ is not. On the other hand at high ISRF both lines will be excited in dense regions, since the clouds are warmer, and in addition, the dissociation of the CO in the diffuse gas will lower the contribution to the emission from $J = 1 - 0$. Overall, the net effect is to increase the value of R_{31} .

R_{31} is usually taken to be $R_{31} = 0.5 \pm 0.2$. Our results show that the scatter of the average value for different clouds is just over the expected error for R_{31} . However, the results in Figure 6 also suggest that using $R_{31} = 0.5$ can considerably underestimate or overestimate the amount of emission associated with W_{10} , and in turn, any derived properties of the source. At the same time this suggests that if the value of the ISRF is known a better constrained conversion factor with a smaller error can be used. We shall explore this in the following Section.

5 DISCUSSION

5.1 X_{CO} in unresolved clouds

The results presented in Section 4 show the dependence of the line ratios on the properties of the gas in the clouds, and the environmental conditions to which the clouds are exposed. In the Milky Way, where it is possible to resolve clouds, the line-ratios can serve as a probe of the physical conditions in the cloud. We have also shown that the area-averaged line-ratios arising from unresolved clouds also show significant variation. This can have implications for how they are used as conversion factors from the $J = 2 - 1$ and $J = 3 - 2$ lines to the more commonly used $J = 1 - 0$ transition that is used in the X-factor. In this section, we explore how these variations in R_{21} and R_{31} affect our derivations of physical clouds properties.

The total column density of H_2 is often calculated by

$$N_{\text{H}_2} = \frac{X_{\text{CO}} W_{21}}{R_{21}}. \quad (3)$$

We therefore want to compare N_{obs} as calculated by Equation 3 with N_{real} , where we take N_{real} to be the column density of H_2 directly from the GADGET-2 snapshot.

Before doing so we reproduce Figure 4 from Clark & Glover (2015) where they plotted the value of X_{CO} for each cloud against the 'star formation rate', which is a proxy for changes in the ISRF and CRIR. In this case we plot against the ISRF as well as include additional clouds that were not studied in Clark & Glover (2015) (See Figure 7). Additionally we have only included clouds with $Z = Z_{\odot}$, since X_{CO} is empirically derived from observations within the Milky Way and therefore intrinsically assumes a solar-like metallicity. It is important to note that this plot may look slightly different from Figure 4 of Clark & Glover (2015). This is because our radiative transfer approach here includes the refinement routine described in Peñaloza et al. (2017) and the Sobolev-Gnedin approximation described in Appendix A. When compared, the results presented here

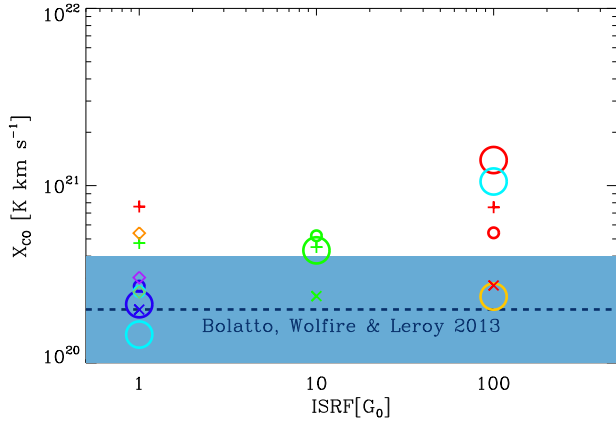


Figure 7. X_{CO} plotted against ISRF for all the clouds using the same labels as in Figure 3. The line represents the typical value for X_{CO} and the shaded region the scatter as given by Bolatto, Wolfire & Leroy (2013). Note that clouds with metallicities of $Z \neq Z_{\odot}$ are not included

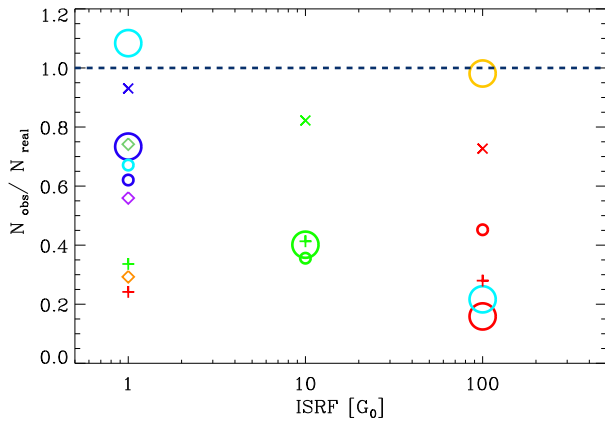


Figure 8. Shows the ratio of $N_{\text{obs}}/N_{\text{real}}$ against ISRF for all the clouds using the same labels as in Figure 3, where N_{obs} is calculated using R_{21} . Note that clouds with metallicities of $Z \neq Z_{\odot}$ are not included

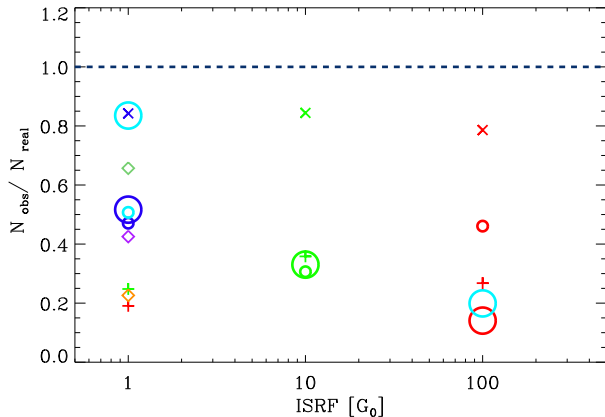


Figure 9. Similar to Figure 8 but using R_{31} instead of R_{21}

systematically lower the value of X_{CO} making these results closer to the typically used value.

In Figure 8 the ratio of $N_{\text{obs}}/N_{\text{real}}$ against the ISRF is plotted. When calculating N_{obs} we have used the $X_{\text{CO}} = 2 \times 10^{20} \text{ cm}^{-2} \text{ K km s}^{-1}$ as given by Bolatto, Wolfire & Leroy (2013) and $R_{21} = 0.7$. From this figure it becomes evident that the amount of molecular gas derived from W_{21} can easily be underestimated. This can be understood when comparing with Figure 7 where at high ISRF the standard value of X_{CO} will underestimate the total column of H_2 . On the other hand Figure 3 shows that using an average value of $R_{21} = 0.7$ will overestimate the amount of W_{10} at high ISRF. Effectively, this compensates the existing biases of both conversion factors to some extent, however this is not enough to avoid underestimating the amount of H_2 due to the high errors in X_{CO} . This is also the case for the green and red plus signs at ISRF = 1, they correspond to the high CRIR runs, where X_{CO} is also underestimated.

At lower ISRF the discrepancies between N_{obs} and N_{real} arise from R_{21} , since at lower ISRF X_{CO} is well within the accepted value. From Figure 3 we can see that using $R_{21} = 0.7$ effectively underestimates the amount of W_{10} and therefore the total column density of H_2 . This effect is even stronger when using R_{31} instead of R_{21} , which is seen in Figure 9 where we use $R_{31} = 0.5$ to calculate N_{obs} .

Finally, even though our results suggest that $R_{21} = 0.7$ is a good first approximation for a conversion factor between W_{21} and W_{10} , the uncertainties and degeneracies surrounding R_{21} still have a significant effect on N_{obs} . This is also true for R_{31} , where the effect on N_{obs} is even larger given that the accepted value for R_{31} is a lower limit according to our results. Alternatively, if the surrounding ISRF could be constrained – for example, by looking at dust SEDs – then the average values in Figure 3 (and Figure 6 for R_{31}) for each ISRF bin could be used to improve the estimate in the value of R_{21} and R_{31} . In principle, this can lead to better true column density of molecular material. Whether this would yield a more accurate value of N_{obs} would depend on the uncertainties on the method used to obtain the ISRF and is beyond the scope of this paper.

5.2 R_{21} as a probe of CO abundance

As discussed in Section 3, variations in the strength of the ISRF and the CRIR affect R_{21} in different ways. Since we are interested in quantifying the effect of the ISRF and the CRIR on the state and abundance of molecular gas we will focus on the following 4 clouds CG15-M4-G1, M4-G1-CR100, M4-G100-CR1 and CG15-M4-G100. We then plot the fractional abundance of CO and H_2 as a function of the average number density of the gas for each cloud. This is shown in Figure 10, where the solid lines represent the H_2 abundance fraction and the dashed line CO abundance fraction.

First thing to note is that the H_2 abundance fraction only changes when the ISRF changes, while changes to the CRIR make a very small impact. Given the chemical model included in these simulations, we know that UV radiation is needed to effectively dissociate H_2 . Even though cosmic rays can destroy some H_2 their overall effect is small (Glover & Clark 2012a). On the other hand cosmic rays can be very effective at reducing the total fraction of CO and

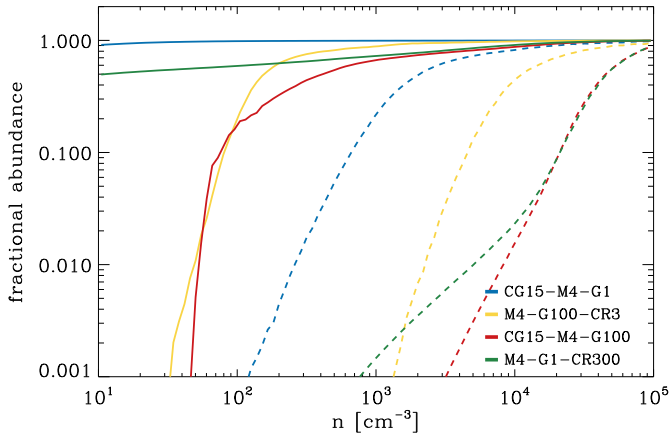
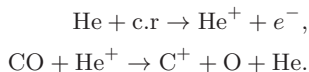


Figure 10. Each coloured line represent a different simulation. Solid lines track, as a function of number density, the fraction of the mass of H in the form of H₂ while dashed lines track the the fraction of the mass of C in the form of CO.

can be seen when comparing the CO abundance of M4-G1-CR100 and M4-G100-CR1. The reason for this becomes evident when looking at the following chemical reactions



When looking at the cloud with high ISRF the fraction of CO abundance (dashed yellow line) increases quickly, this is because once the CO is well shielded the production of CO is efficient. As a result the emission coming from these high-density regions will be bright and well correlated with high values of R_{21} . On the other hand when looking at the high CRIR cloud, the fraction of CO abundance (dashed green line) starts increasing at similar number densities ($\sim 10^3 \text{ cm}^{-3}$), however, at a much slower rate. This is because the CO production is being constantly hampered by the cosmic rays which are not attenuated. As such the emission from these regions will be faint due to the low abundance of CO, more importantly R_{21} will have values around ~ 0.3 . In addition, the increase in the CRIR will heat up the gas and therefore slightly increase the average value of R_{21} (See Figure 3).

A recent paper by Bisbas et al. (2017) studied how increasing the CRIR can be important in destroying CO. In Figure 11 of this paper they compare the CO/H₂ fraction as a function of number density, for varying CRIR. We reproduce this figure with our own set of simulations for which the CRIR is increased in the same way (Note to better compare to their results we ran an additional simulation with $\zeta_{\text{H}} = 3 \times 10^{-14} \text{ s}^{-1}$ that was not included in our initial setup). Our results show a similar trend where the CO/H₂ abundance ratio decreases with increasing CRIR.

The effect of CRIR on the abundance of CO will have a direct impact on the CO emission and therefore how much molecular gas can be traced within GMCs. Even though the total CO emission is reduced, our synthetic observations show that the changes in abundances seen above can be traced to some extent when looking at the resolved integrated intensities and R_{21} of these clouds (see Figure 2).

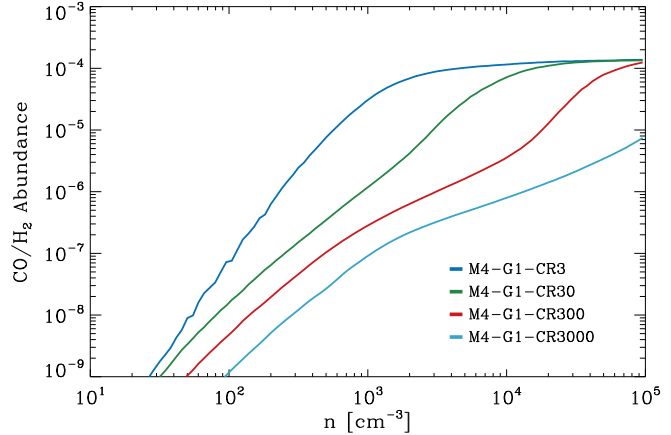


Figure 11. Illustrates how CO/H₂ abundance ratio changes with average number density.

One caveat to keep in mind when considering these results, is that our models have a constant CRIR throughout the whole cloud – cosmic rays are not attenuated and therefore able to reach the densest regions of the cloud. Whether this is an accurate approximation is beyond the scope of this study and therefore the reader should keep this in mind when interpreting these results.

6 CONCLUSIONS

We have studied a range of numerical models of molecular clouds, in which the initial cloud parameters, and properties of the ISM, were systematically varied. We performed radiative transfer calculations on the simulations just before the onset of star formation in each case, to create synthetic CO line emission cubes for all clouds. We used these synthetic observations to study the impact of environment on CO line emission and CO line ratios. Our main findings can be summarised as follows:

(i) The value of R_{21} and its correlation with dense/cold and warm/diffuse, allows it to act as a probe of the conditions of the gas within GMCs. From all the environmental changes studied, variations in the ISRF and the CRIR have the largest impact on the average value and the cumulative PDF of R_{21} .

(ii) The dependence of different line-ratios (R_{21} , R_{32} and R_{31}) on environment can also be observed when looking at unresolved clouds where the total emission is averaged. Our results suggest that the accepted values for R_{21} and R_{31} are a good first approximation. At the same time the scatter around the accepted value ($\sim \pm 0.2$) suggests that careful consideration should be had when using them as conversion factors, specially given the high dependence on the ISRF.

(iii) When calculating the column density of H₂ molecular gas of GMCs it is important to consider the biases of X_{CO} and line ratios R_{21} and R_{31} . At a high ISRF ($G_0 = 100$) X_{CO} will underestimate N_{H_2} . This is only slightly compensated by the bias line ratios have at high ISRF. On the other hand since at low ISRF ($G_0 = 1$) X_{CO} is well constrained, the errors in N_{H_2} come from line ratios underestimating the total amount of emission from the $J = 1 - 0$ transition line.

(iv) Cosmic rays can help regulate the total CO abundance within GMCs. When $\zeta_{\text{H}} = 3 \times 10^{-17} \text{ s}^{-1}$ the CO to H₂ abundance ratio is $\sim 10^{-4}$ at densities of $\sim 10^3 \text{ cm}^{-3}$. As ζ_{H} is increased the CO to H₂ fraction is considerably reduced reaching values of only $\sim 10^{-5}$ at densities of $\sim 10^5 \text{ cm}^{-3}$ for rates of $\zeta_{\text{H}} = 3 \times 10^{-14} \text{ s}^{-1}$. This has a direct impact on the CO emission and on the average value and distribution of R_{21}

ACKNOWLEDGEMENTS

PCC acknowledges support from the Science and Technology Facilities Council (under grant ST/N00706/1) and the European Community's Horizon 2020 Programme H2020-COMPET-2015, through the StarFormMapper project (number 687528). SCOG and RSK acknowledge financial support from the Deutsche Forschungsgemeinschaft via SFB 881, "The Milky Way System" (sub-projects B1, B2 and B8) and SPP 1573, "Physics of the Interstellar Medium". They also acknowledge support from the European Research Council under the European Community's Seventh Framework Programme (FP7/2007-2013) via the ERC Advanced Grant STARLIGHT (project number 339177).

REFERENCES

- Aravena M. et al., 2010, ApJ, 718, 177
 Aravena M. et al., 2014, MNRAS, 442, 558
 Barnes P. J., Muller E., Indermuehle B., O'Dougherty S. N., Lowe V., Cunningham M., Hernandez A. K., Fuller G. A., 2015, ApJ, 812, 6
 Barriault L., Joncas G., Plume R., 2011, MNRAS, 416, 1250
 Bauermeister A. et al., 2013, ApJ, 768, 132
 Benz W., 1990, in Numerical Modelling of Nonlinear Stellar Pulsations Problems and Prospects, Buchler J. R., ed., p. 269
 Bertram E., Glover S. C. O., Clark P. C., Klessen R. S., 2015, MNRAS, 451, 3679
 Bigiel F., Leroy A., Walter F., Brinks E., de Blok W. J. G., Madore B., Thornley M. D., 2008, AJ, 136, 2846
 Bigiel F. et al., 2016, ApJL, 822, L26
 Bisbas T. G., Papadopoulos P. P., Viti S., 2015, ApJ, 803, 37
 Bisbas T. G., van Dishoeck E. F., Papadopoulos P. P., Szűcs L., Bialy S., Zhang Z.-Y., 2017, ApJ, 839, 90
 Bolatto A. D., Wolfire M., Leroy A. K., 2013, ARA&A, 51, 207
 Brand J., Wouterloot J. G. A., 1995, A&A, 303, 851
 Casoli F., Dupraz C., Combes F., Kazes I., 1991, A&A, 251, 1
 Clark P. C., Glover S. C. O., 2015, MNRAS, 452, 2057
 Clark P. C., Glover S. C. O., Klessen R. S., 2012, MNRAS, 420, 745
 Daddi E. et al., 2015, A&A, 577, A46
 Dullemond C. P., 2012, ASCL, 1202.015
 Eckart A., Downes D., Genzel R., Harris A. I., Jaffe D. T., Wild W., 1990, ApJ, 348, 434
 Federrath C., Roman-Duval J., Klessen R. S., Schmidt W., Mac Low M.-M., 2010, A&A, 512, A81
 Glover S. C. O., Clark P. C., 2012a, MNRAS, 421, 116
 Glover S. C. O., Clark P. C., 2012b, MNRAS, 421, 9
 Glover S. C. O., Clark P. C., 2016, MNRAS, 456, 3596
 Glover S. C. O., Mac Low M.-M., 2007a, ApJS, 169, 239
 Glover S. C. O., Mac Low M.-M., 2007b, ApJ, 659, 1317
 Glover S. C. O., Smith R. J., 2016, MNRAS, 462, 3011
 Gnedin N. Y., Tassis K., Kravtsov A. V., 2009, ApJ, 697, 55
 Habing H. J., 1968, Bull. Astron. Inst. Netherlands, 19, 421
 Hartwig T., Clark P. C., Glover S. C. O., Klessen R. S., Sasaki M., 2015, ApJ, 799, 114
 Hasegawa T., 1997, in IAU Symposium, Vol. 170, IAU Symposium, Latter W. B., Radford S. J. E., Jewell P. R., Mangum J. G., Bally J., eds., pp. 39–46
 Kennicutt, Jr. R. C., 1998, ApJ, 498, 541
 Klessen R. S., Glover S. C. O., 2016, Star Formation in Galaxy Evolution: Connecting Numerical Models to Reality, Saas-Fee Advanced Course, Volume 43. ISBN 978-3-662-47889-9. Springer-Verlag Berlin Heidelberg, 2016, p. 85, 43, 85
 Leroy A. K. et al., 2009, AJ, 137, 4670
 Nelson R. P., Langer W. D., 1999, ApJ, 524, 923
 Nishimura A. et al., 2015, ApJS, 216, 18
 Offner S. S. R., Bisbas T. G., Bell T. A., Viti S., 2014, MNRAS, 440, L81
 Ossenkopf V., 1997, New Astronomy, 2, 365
 Papadopoulos P. P., van der Werf P., Xilouris E., Isaak K. G., Gao Y., 2012, ApJ, 751, 10
 Peñaloza C. H., Clark P. C., Glover S. C. O., Shetty R., Klessen R. S., 2017, MNRAS, 465, 2277
 Pellegrini E. W. et al., 2013, ApJL, 779, L19
 Pon A. et al., 2016, ApJ, 827, 107
 Sakamoto S., Hasegawa T., Handa T., Hayashi M., Oka T., 1997, ApJ, 486, 276
 Sakamoto S., Hayashi M., Hasegawa T., Handa T., Oka T., 1994, ApJ, 425, 641
 Sandstrom K. M. et al., 2013, ApJ, 777, 5
 Sawada T. et al., 2001, ApJS, 136, 189
 Schinnerer E. et al., 2013, ApJ, 779, 42
 Schmidt M., 1959, ApJ, 129, 243
 Shetty R., Glover S. C., Dullemond C. P., Klessen R. S., 2011, MNRAS, 412, 1686
 Sobolev V. V., 1957, SOVAST, 1, 678
 Springel V., 2005, MNRAS, 364, 1105
 van der Tak F. F. S., Black J. H., Schöier F. L., Jansen D. J., van Dishoeck E. F., 2007, A&A, 468, 627
 Vlahakis C., van der Werf P., Israel F. P., Tilanus R. P. J., 2013, MNRAS, 433, 1837
 Walch S. et al., 2015, MNRAS, 454, 238

APPENDIX A: SOBOLEV-GNEDIN APPROXIMATION

The Sobolev approximation, most commonly known as the Large Velocity Gradient (LVG) approximation, is widely used when calculating the level populations of a gas within GMCs. In the original paper, Sobolev (1957) studied the idea that emission coming from gas within a moving medium will be doppler-shifted before it can be reabsorbed and therefore escapes. Whether a photon escapes or not is determined by the velocity gradient ($|\nabla \vec{v}|$), i.e. the larger $|\nabla \vec{v}|$ is the

smaller is the volume where the photon can be reabsorbed. RADMC-3D already makes use of the Sobolev approximation when calculating level populations, the detailed implementation can be found in Shetty et al. (2011).

Even though Ossenkopf (1997) showed that the Sobolev approximation is a robust approximation for GMCs, the method is still limited by the fact that it only considers changes in velocity. When using the Sobolev approximation the aim is to calculate the probability that a photon will escape a given region. The escape probability is given by:

$$\beta = \frac{1 - e^{-\tau_v}}{\tau_v}, \quad (\text{A1})$$

where τ_v is the optical depth given a velocity gradient. τ_v can be calculated by

$$\tau_v = \frac{c^3}{8\pi\nu_{ij}^3} \frac{A_{ij}n}{1.064|\nabla\vec{v}|} \left(f_j \frac{g_i}{g_j} - f_i \right), \quad (\text{A2})$$

where ν_{ij} is the emission frequency of the transition, g_i and g_j are the statistical weights for each level, n the total number density and, f_i and f_j is the fractional population level (van der Tak et al. 2007).

Now consider a scenario in which $|\nabla\vec{v}|$ is small but the change in density i.e. the density gradient ($|\nabla\rho|$) is high. According to Equation A2 τ would be high and therefore the probability of a photon escaping would be low. However given that $|\nabla\rho|$ is higher the escape probability of the photon should be higher, yet Equation A2 does not consider $|\nabla\rho|$ and therefore the escape probability is unchanged. For the GMCs considered in this study we can foresee different cloud regions where this scenario is likely: dense cores can have low velocity dispersions, yet can have very steep density gradients. In effect, the LVG is a local approximation, in that it constructs a length-scale based on local properties. These local properties, such as density, temperature, etc, are then assumed to be held constant over this length-scale, allowing us to derive an optical depth. If, however, the density varies rapidly, then the LVG approximation makes an error. Thankfully, it is relatively simple to improve this approximation.

Gnedin Length Approximation

The Sobolev approximation is a local approximation given a certain length scale, where the length scale is calculated from the velocity gradient. Commonly this is called the Sobolev length and is defined by:

$$L_{Sob} = \frac{v_{th}}{|\nabla\vec{v}|}, \quad (\text{A3})$$

where v_{th} is the thermal velocity. From this and equation A2 one can reconstruct a more general solution for the opacity where L need not be L_{Sob} but any other length scale relevant to the problem at hand. One such length scale is the one presented by Gnedin, Tassis & Kravtsov (2009) where they define a length scale base on density gradients in order to determine column densities of H_2 . They define this length scale as

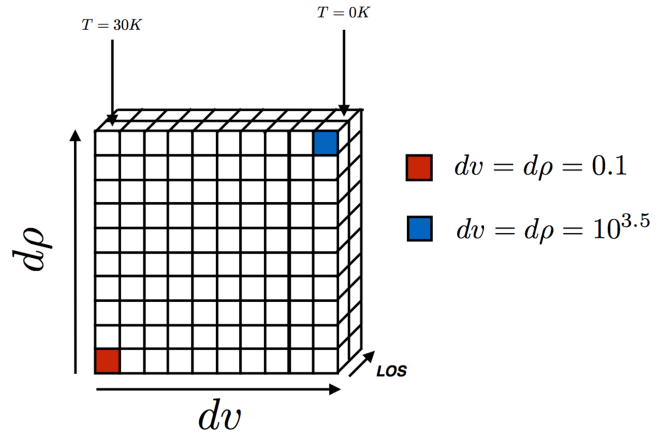


Figure A1. The setup of the grid used as an input for the radiative transfer. All the cells in the the front slice have the same density, temperature and velocity. The back slice has a temperature of 0 K. Densities and velocities take a value according to dv or $d\rho$, which are increased such that $dv = d\rho$ over the diagonal. dv is increased accordingly over the x -axis and $d\rho$ over the y -axis.

$$L_{Gn} = \frac{n_{\text{H}_2}}{|\nabla n_{\text{H}_2}|}, \quad (\text{A4})$$

where n_{H_2} is the number density of H_2 , however for our purposes we may define this in terms of the number density of the molecule that is being modelled. With this in mind we can rewrite equation A2, to calculate an optical depth (τ_ρ) given a density gradient by

$$\tau_\rho = \frac{hc}{4\pi\sqrt{\pi}v_{th}} \frac{n^2}{|\nabla n|} \left(f_j \frac{g_i}{g_j} - f_i \right), \quad (\text{A5})$$

that has the same form as Equation A2. At the same time Equation A5 would fail to accurately calculate the escape probability given that τ_ρ does not consider the gradient in velocity, especially in highly turbulent systems such as GMCs.

At this point we have two adequate yet limited ways of calculating an optical depth. To obtain the best from each we follow the approach taken by Hartwig et al. (2015), where they take the harmonic mean between τ_v and τ_ρ , as follows

$$\tau = \frac{\tau_v\tau_\rho}{\tau_v + \tau_\rho}. \quad (\text{A6})$$

The resulting optical depth will then be used in equation A1 to calculate the escape probability.

Implementation and Testing

We have used the underlying framework of RADMC-3D and implemented the Gnedin approximation, as described above, as an improvement to the already present Sobolev approximation. In order to test this method we set up a test scenario that highlights the difference between LTE, LVG and LVG+ (Sobolev-Gnedin approximation).

We set up an input grid of 10 by 10 by 2, Figure A1 shows the position-position-position (PPP) cube that was used as an input into RADMC-3D. All the cells in the front

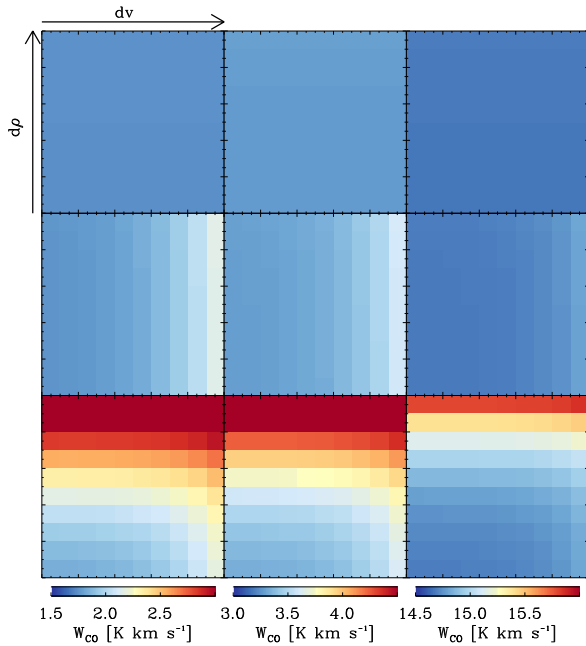


Figure A2. The integrated intensities of CO $J = 1 - 0$ for each run on each cube. Each row has a different method for calculating level populations: top = LTE, middle = LVG, bottom = LVG+. Similarly each column has a different number density for the front slice, left: $n = 50 \text{ cm}^{-3}$, middle: $n = 100 \text{ cm}^{-3}$, right: $n = 500 \text{ cm}^{-3}$. Note that even though the colours are similar the colourbar for each column is different

slice have the same physical properties and will therefore have the same intrinsic emission in a scenario where $|\nabla \vec{v}|$ or $|\nabla \vec{\rho}|$ are not considered. The back slice serves to calculate the velocity and density gradients used to obtain the optical depth of each cell in the front slice. To keep the setup simple, we increase $|\nabla \vec{v}|$ only in the x -axis while keeping $|\nabla \vec{\rho}|$ constant. Conversely we increase $|\nabla \vec{\rho}|$ while keeping $|\nabla \vec{v}|$ constant on the y -axis. The increase in the gradient is taken with respect to the values of density and velocity in the front slice. These are such that $dv = d\rho$ will be the same whenever $x = y$. Additionally to avoid confusion we set the temperature of each cell in the back slice to be $T = 0 \text{ K}$ so that these cells have no emission.

Given the purpose of this paper, we perform the radiative transfer for CO $J = 1 - 0$ but in principle the method works for any other molecule or line. Additionally we create 3 different cubes for 3 different densities of the front slice ($n = 50 \text{ cm}^{-3}$, $n = 100 \text{ cm}^{-3}$ and $n = 500 \text{ cm}^{-3}$). We run 3 radiative transfer simulations for each cube, each of these uses either LTE, LVG or LVG+. The resulting integrated intensities for each run for each cube are shown in Figure A2.

As expected changing the method for calculating the population levels makes a big difference in the final image. Since the density and temperature of each cell are exactly the same assuming LTE results in the integrated intensity for each cell also being the same. This is because LTE uses no information of the gradient surrounding the cell to calculate the level populations. For the LVG scenario we can definitely see a change in intensity over the x -axis, which corresponds to an increase in $|\nabla \vec{v}|$. However not taking $|\nabla \vec{\rho}|$ into account

results in the intensity being exactly the same on the y -axis. Finally when using the LVG+ method both changes on $|\nabla \vec{v}|$ and $|\nabla \vec{\rho}|$ are reflected on the final intensity of each cell.

One important note to keep in mind when looking at these results is why increasing the gradient results in an increase in intensity rather than a decrease. The reason is that the background radiation and the high temperature of the cell causes higher levels to be radiatively pumped. These will then quickly cascade down to the the ground state i.e $J = 1 - 0$ causing it to be much brighter. The reason behind this is that for lower temperatures the difference between cells is very small and hard to see. This should not be a problem since our interest is to test that the method works. In the next Section we will show how using LVG+ changes the integrated intensities of one of our clouds.

Result Comparison

Even though we tested that LVG+ works, it is important to check whether this new method has any significant effect on a more realistic system such as our numerically simulated clouds. To check this we performed two radiative transfer simulations on CG15-M4-G1, one using LVG and another using LVG+. The integrated intensities of these two runs are shown in Figure A3.

At first glance it seems that the difference between LVG and LVG+ is negligible. However when taking the ratio between the both we can see that the brightness of the cloud definitely changes when using LVG+. For most regions of the cloud the brightness is reduced, nonetheless there are still regions that can either become brighter or remain the same. It then follows that considering changes in the local density does play an important role when calculating the level populations and total emission of a system. This illustrates how small changes in the physical conditions of the gas and the interplay with the surrounding environment can lead to changes in the total emission.

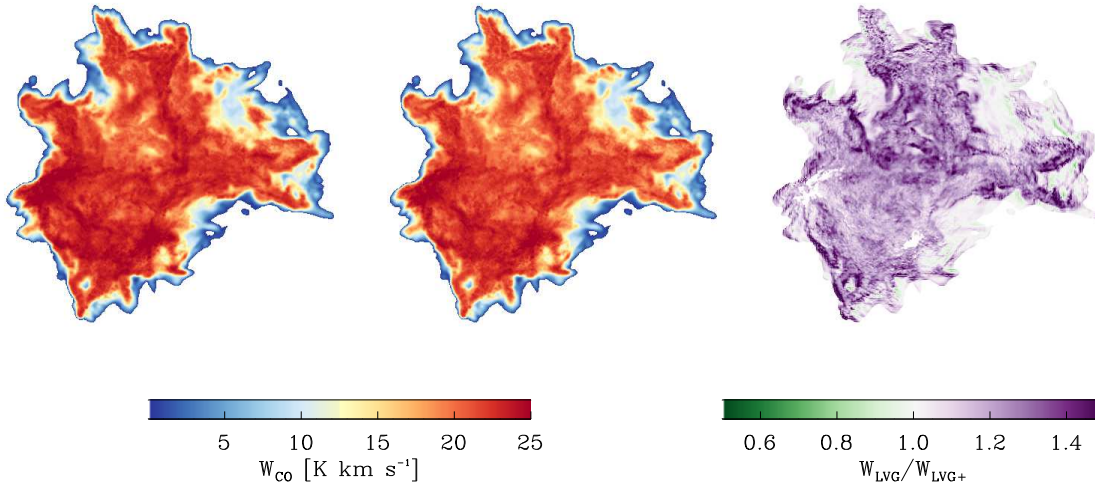


Figure A3. The image on the left shows the integrated intensity for CG15-M4-G1 with an LVG treatment while the middle image does so for LVG+. The image on the right is the ratio of LVG/LVG+ integrated intensities